

INLET EFFECTS ON VERTICAL-DOWNWARD AIR-WATER TWO-PHASE FLOW

S. Qiao, D. Mena, and S. Kim*

Department of Mechanical and Nuclear Engineering
The Pennsylvania State University
230 Reber Building, University Park, PA 16802, USA
szq105@psu.edu; dnm5125@psu.edu; skim@psu.edu

ABSTRACT

This paper focuses on investigating the geometric effects of inlets on global and local two-phase flow parameters in vertical-downward air-water two-phase flow. Flow visualization, frictional pressure loss analysis, and local experiments are performed in a test facility constructed from 50.8 mm inner diameter acrylic pipes. Three types of inlets of interest are studied: (1) two-phase flow injector without a flow straightener (Type A), (2) two-phase flow injector with a flow straightener (Type B), and (3) injection through a horizontal-to-vertical-downward 90° vertical elbow (Type C). A detailed flow visualization study is performed to characterize flow regimes including bubbly, slug, churn-turbulent, and annular flow. Flow regime maps for each inlet are developed and compared to identify the effects of each inlet. Frictional pressure loss analysis shows that the Lockhart-Martinelli method is capable of correlating the frictional loss data acquired for Type B and Type C inlets with a coefficient value of $C=25$, but additional data may be needed to model the Type A inlet. Local two-phase flow parameters measured by a four-sensor conductivity probe in four bubbly and near bubbly flow conditions are analyzed. It is observed that vertical-downward two-phase flow has a characteristic center-peaked void profile as opposed to a wall-peaked profile as seen in vertical-upward flow. Furthermore, it is shown that the Type A inlet results in the most pronounced center-peaked void fraction profile, due to the coring phenomenon. Type B and Type C inlets provide a more uniform distribution of the void fraction profile with a reduced coring effect.

KEYWORDS

Inlet effects, vertical-downward two-phase flow, flow regime map, local two-phase flow parameters, frictional pressure drop

1. INTRODUCTION

Two-phase flow is a widely observed phenomenon present in many engineering applications such as nuclear reactors as well as industrial systems. Most of these practical applications have different sizes of coolant channels in varying orientations with different types of inlets, all of which can affect the two-phase flow characteristics. The inlet configurations specifically can induce significant changes in the interfacial structures and their transport phenomena. Since the mass, momentum, and energy transfer between the two phases are greatly influenced by changes in the interfacial structures, experimental studies are crucial in improving the understanding of the inlet effects on two-phase flow.

A number of researchers have investigated two-phase flow in vertical-downward channels over the decades. Oshinowo and Charles [1] performed vertical downward air-water and air-glycerol two-phase flow experiments in 25.4 mm pipes interconnected with a U bend. They observed and defined six flow regimes: bubbly-coring, bubbly-slug, falling film, falling bubbly-film, froth flow, and annular flow. Data from the investigation was used to formulate an empirical flow pattern correlation for both upward and downward flow. Usui and Sato [2] also performed air-water two-phase flow visualization in vertical downward pipe with a U bend. They identified bubbly, slug, churn and annular flow regimes. A correlation was developed to predict the average void fraction for each flow regime and flow regime transition criteria based on two-phase flow data acquired by a conductivity probe. Barnea et al. [3] performed flow visualization in 25.4 mm and 50.8 mm vertical downward and inclined pipes. Flow regime maps for various downward inclinations and a model for predicting flow pattern boundaries were developed.

More recently, Goda et al.[4,5], studied the adiabatic, air–water, co-current, vertically downward two-phase flow in round pipes with internal diameters of 25.4 and 50.8 mm. Flow regime maps were obtained using characteristic signals acquired by an impedance void meter and a neural network-based identification methodology. Their study was then continued by Ishii et al. [6], and Kim et al. [7]. Characteristics of the local interfacial structures and bubble interaction mechanisms were studied. In addition, the interfacial area transport equation applicable to downward flow was developed with certain modifications in bubble interaction terms on the basis of interfacial area transport for upward flows. Bhagwat and Ghajar [8] performed flow visualization studies in both vertical-upward and vertical-downward two-phase flow as well as an analysis of the performance of various void fraction correlations available in the literature.

From the discussion above, most of the previous work has focused either on flow regime map development and prediction, the effects of channel orientation, or the interfacial structures in downward two-phase flow. In the studies, various types of inlets, such as U-bend and double-annulus injector type, were used for the injection of two-phase flow into the test section. As one can imagine, different inlets can produce different two-phase flow patterns at the inlet that will develop uniquely across the test section.

However, there have been no systematic efforts made to study the effects of different inlet configurations on flow regime transitions and the interfacial structures along the development length. In view of this, the objectives of the current study are to characterize effects of inlet on downward two-phase flow via: (1) identification of flow regimes and regime transition boundaries for each inlet, (2) two-phase frictional pressure loss analysis for each inlet using Lockhart-Martinelli method, and (3) analysis on the development of local interfacial structures for each inlet.

2. EXPERIMENTAL FACILITY AND TEST CONDITIONS

The experiments are performed in an adiabatic air-water test facility, which consists of vertical and horizontal test sections made out of 50.8 mm inner diameter acrylic pipes interconnected by 90° vertical glass elbows. A schematic diagram of the test facility is shown in Fig. 1. The elbows have a radius of curvature of 152.4 mm. The lengths of the vertical and horizontal section are 3.35 and 9.45 m, yielding development lengths of 66 and 186 diameters, respectively. Along the test section, 24 measurement locations are available with a total of 15 movable instrumentation ports. These measurement ports are designed to facilitate local conductivity probe measurements, pressure measurements, and flow visualization. The vertical test sections are capable of three types of inlet configurations for vertical-downward two-phase flow. These include: (1) two-phase flow injector without a flow straightener (Type A), (2) two-phase flow injector with a flow straightener (Type B), and (3) horizontal-to-vertical-downward flow through a 90° vertical elbow (Type C).

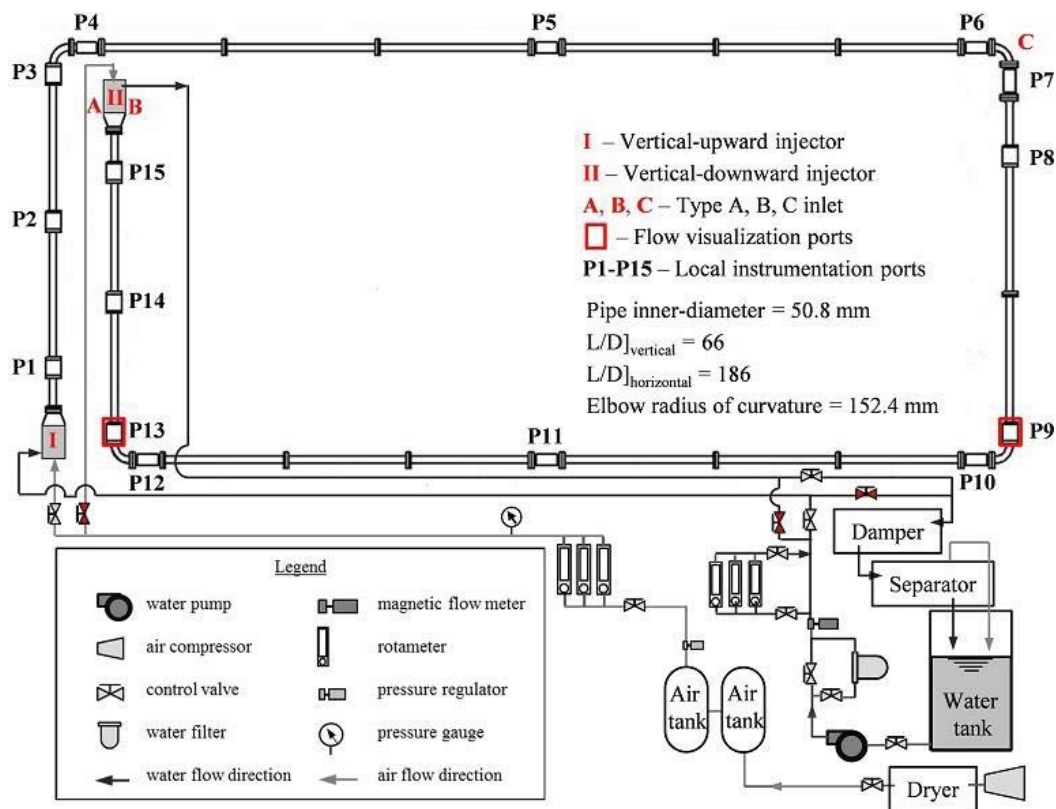


Figure 1. Simplified schematic diagram of the test facility.

To create the two-phase flow, filtered water is supplied to the test section from an accumulator tank with a capacity of ~2300 L by a centrifugal pump. The water flow rate is measured by a two-wire electromagnetic flowmeter with an accuracy of $\pm 5\%$ of the full-scale reading. Air is supplied to the system by an air compressor at a pressure of 689 kPa via a two-stage air accumulation system which is employed to minimize any pressure fluctuations in the air being supplied to the two-phase injection units. The air flow rate is measured by a set of rotameters with an accuracy of $\pm 3\%$ of the full-scale reading. The two-phase mixture is created by a two-phase injection system consisting of a double annulus configuration, as shown in Fig. 2(a). Two sintered spargers (one for each flow direction) are used to inject nearly uniform bubbles of 2 - 3 mm, at either end of the test loop. The spargers are centered within an annulus that allows for two separate inlet liquid flow rates. The inner liquid flow rate is held constant and is designed to shear off nearly uniform bubbles whereas the outer liquid flow is used to regulate the global flow rate within the facility. The outer annulus, which serves as the primary liquid injection line, is further separated into three equally spaced inlets of 120° in order to prevent the formation of vortices and to provide a uniform supply of liquid in the injection unit. A converging conical section is used to connect the injection unit with a diameter of 76.2 mm to the 50.8 mm inner diameter pipe. Moreover, a honeycomb-type flow straightener placed on the outer annulus of the injection unit is used to differentiate between the Type A and Type B injection systems investigated in the current study. Fig. 2 (b) shows the schematic diagram of elbow used for Type C inlet. The elbow has a non-dimensional radius of curvature of $R_c/D = 3$. During the experiment, two-phase flow from the horizontal section enters the elbow then comes out in a vertical-downward direction. A differential pressure transducer is used to obtain pressure measurements along the test section. The accuracy of the pressure transducer is $\pm 0.5\%$ between 0.75 kPa and 5 kPa, and $\pm 0.1\%$ between 5 kPa and 50 kPa.

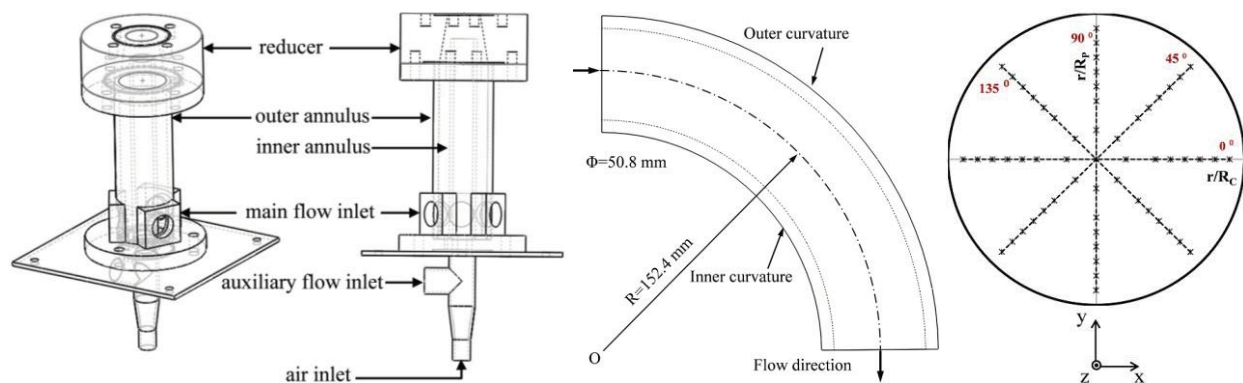


Figure 2. Schematic diagram of (a) two-phase flow injector, (b) 90° vertical elbow, and (c) measurement mesh used at port P7 ($L/D=3$) along four radial directions.

A high-speed video camera with a resolution of 512x512 is used to perform flow visualization studies to develop flow regime maps for all three types of inlets. The frame rate of a high-speed video camera is set to 2000 or 4000 fps throughout the experiment depending on the flow conditions. The shutter speed is set to 1/10000 sec. A total of 360, 140, and 170 videos are taken for Type A, B inlets at port P13, and for Type C inlet at port P7, respectively, as highlighted in Fig. 1. The experimental flow conditions vary within $-j_f = 0.2$ to 4.0 m/s and $-j_{g,loc} = 0.01$ to 6.0 m/s. Here, the negative signs indicate the downward direction of the flow.

The state-of-the-art four-sensor conductivity probe [9] is used to measure time-averaged local two-phase flow parameters which include void fraction α , bubble frequency f_b , bubble velocity v_g , and interfacial area concentration a_i . A traversing unit with a resolution of 0.01 mm is used to accurately position the conductivity probe at different radial locations within the pipe cross section. The data are obtained at a sampling rate of 50 kHz for 60 s.

The experiments are performed at room temperature 20 °C and near ambient pressure. A total of four different combinations of gas and liquid flow rates, as listed in Table I, are investigated for each inlet type. In the table, $j_{g,loc}$ indicates the gas superficial velocity at the port located farthest away from the inlet. The flow conditions are selected to be within or near the bubbly flow regime based on the flow regime maps presented in this study. Conductivity probe measurements are performed at ports P13 to P15 for Types A and B inlets, and at ports P7 to P9 for the Type C inlet. It is observed that at port P7 the flow is asymmetrical; therefore, local data is acquired in four different radial directions (i.e., 0°, 45°, 90°, 135°), as shown in Fig. 2(c), by rotating the measurement port. The direction of the flow is out of the page and r/R_p and r/R_c denote the non-dimensional radial axes perpendicular to and along the curvature of the elbow, respectively. The radius towards the outer elbow curvature and the fluid flow direction are taken as positive. At the other ports the flow is assumed to be axisymmetric so the data is obtained along one diameter of the pipe cross section.

Table I. Flow conditions

Run No.	Run 1	Run 2	Run 3	Run 4
$-j_f$ [m/s]	4.00	4.00	4.00	4.00
$-j_{g,loc}$ [m/s]	0.108	0.165	0.284	0.399

3. RESULTS AND DISCUSSION

The discussion of the experimental results is divided into three sections: flow visualization, two-phase frictional pressure loss analysis, and local interfacial structures analysis.

3.1. Flow Visualization

Flow visualization is a useful and intuitive method to study two-phase flow. For upward flow, it is generally accepted that there exists four distinct flow regimes, i.e., bubbly, slug, churn-turbulent and annular flow. However, for downward flow, the definitions of the flow regimes and the flow regime transition boundaries are not well defined. In view of this, flow visualization is performed to study the downward two-phase flow characteristics. Videos are recorded through acrylic transparent ports at $L/D = 55.5$ for Type A and Type B inlets and at $L/D = 67.5$ for Type C inlet, where the flow can be assumed to be developed. Four flow regimes similar to vertical-upward two-phase flow are identified.

3.1.1. Definition of vertical-downward two-phase flow regimes

Fig. 3 (a)-(d) show four flow regimes that typically occur in vertical-downward two-phase flow. The definitions of these flow regimes are given below.

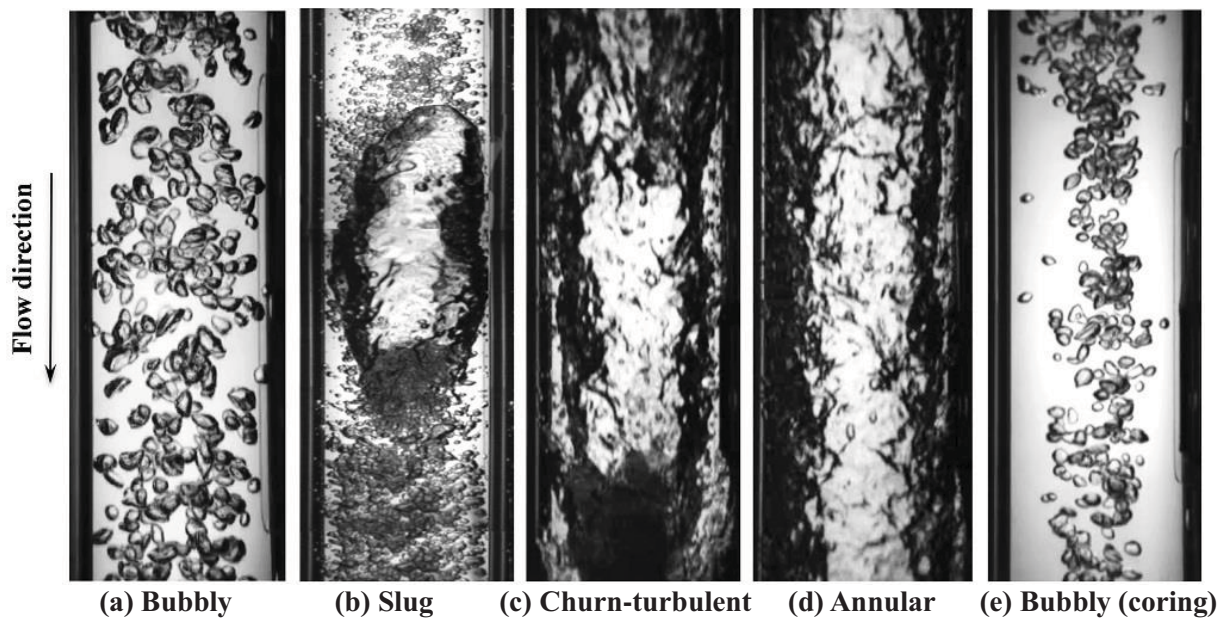


Figure 3. Images for each flow regime captured from flow visualization.

(a) *Bubbly Flow.* The characteristics of bubbly flow are similar to that in the upward flow. The bubbles are spherical or ellipsoidal in shape and nearly uniform in sizes and dispersed in the continuous liquid phase. One of the unique features in downward bubbly flow is the coring phenomenon in which bubbles migrate towards the center of the pipe and rotate as they move along the axial length of the test section. This phenomenon occurs due to the lift and wall repulsion forces pushing the bubbles toward the pipe centerline. A characteristic image of the coring in downward bubbly flow is shown in Fig. 3(e). This phenomenon is also confirmed by previous studies[1,2,4]. In the current study, this coring phenomenon is observed in conditions where the liquid-phase Reynolds number is greater than 10^5 ($|j_f| > 2.0$ m/s).

(b) *Slug Flow*. Slug flow shows rather different characteristics from that in upward flow. In downward flow, liquid slug moves downward followed by elongated slug bubble. The slug bubble typically has an off-centered nose pointing opposite to the flow direction and the chord length of the slug bubble is greater than the pipe diameter. Near the tail region, small bubbles are sheared off from the rim and a wake region is formed.

(c) *Churn-Turbulent Flow (C-T)*. Churn-turbulent flow also shows quite different characteristics from that in upward flow. This flow regime can generally be considered as the transition between slug and annular flow. In this flow regime, a highly distorted gas slug occupies the whole pipe diameter while highly chaotic liquid slug exists between consecutive gas slugs. A wavy liquid film that entrains small bubbles is formed near the wall. Also unique to churn-turbulent is the appearance of flow reversal occurring in the wake region in front of the C-T bubble.

(d) *Annular Flow*. Downward annular flow is similar to that in upward flow in that it is characterized by a continuous gas core with droplet entrainment and continuous wavy liquid film near the wall. In downward flow, annular flow can be subdivided into two categories: falling film flow and annular drop flow [4]. Falling film flow occurs when sufficient water cannot be supplied to fill the test section. Annular drop flow is similar to the annular flow observed in upward flow, which is formed at high gas flow rate. In the current study, falling film flow and annular drop flow are not differentiated.

3.1.2. Flow regime map

Based on the defined flow regimes described above, the recorded videos for different flow conditions are classified to different flow regimes to characterize effects of inlet on flow regimes and regime transition boundaries for each inlet. The developed flow regime maps are compared with each other as well as that available in the literature. In the comparison, the Type A inlet is used as reference.

Fig. 4(a) shows the flow regime map for the Type A inlet. The flow regime map is separated into four flow regime regions. The area colored in gray indicates the “kinematic shock” which occurs near the injector. Kinematic shock is an unstable phenomenon with a shock front separated by an unstable interface between two distinct regions, i.e. annular flow in the upstream and bubbly flow in the downstream. Even with the existence of kinematic shock, stable flow regimes are observed in the downstream port P13. Therefore, the kinematic shock region is eliminated from the following discussion in this paper. The flow regime map is compared with that developed by Goda et al. [4], as shown in Fig. 4(b), noting that no flow straightener was employed in their study. It is observed that both the transition boundaries between churn-turbulent to annular flow and slug to churn-turbulent flow agree well with each other. The main difference comes from the transition boundary from bubbly to slug flow. The current flow regime map indicates that transition from bubbly to slug flow occurs at higher superficial gas velocity when the superficial liquid velocity is smaller than 2.5 m/s. This may be caused by differences in injector configurations.

For the Type B inlet, a flow straightener is added to the injector to minimize any rotation induced by the injector design and to provide a more uniform liquid flow. The flow regime map developed for such inlet is shown in Fig. 5(a), and the comparison of the flow regime map between Type A and Type B inlets is shown in Fig. 5(b). Overall, the two types of inlets show similar transition characteristics. Two major differences are observed, namely: (1) the kinematic shock phenomenon near the injector disappears after installing the flow straightener in the injector; (2) all the transition boundaries are shifted towards higher superficial gas velocities. This is because the flow straightener reduces the rotation and the coring phenomenon that contributes to the coalescence of dispersed bubbles into slug bubbles.

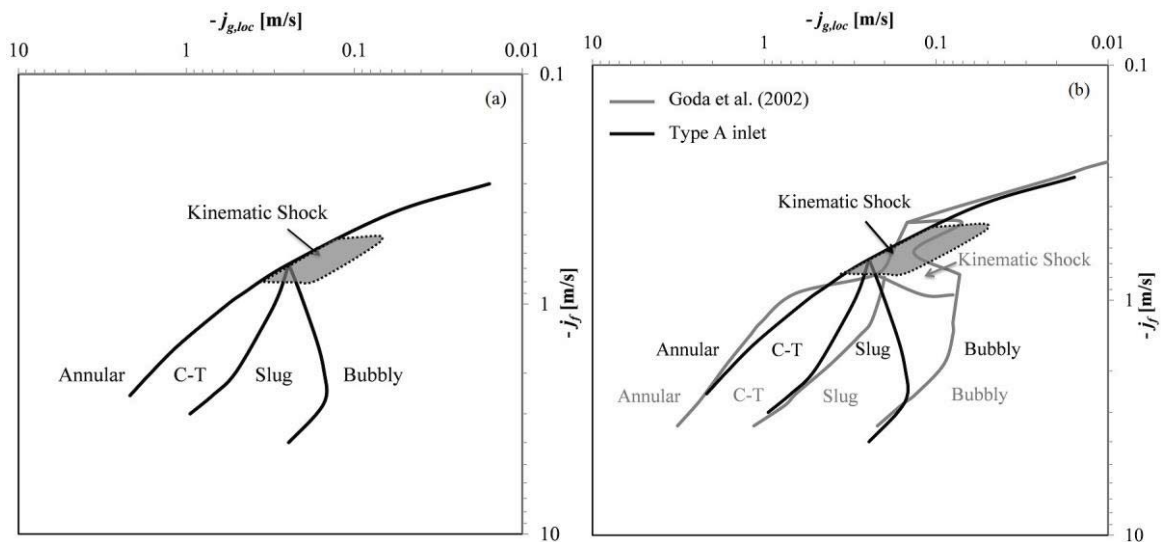


Figure 4. (a) Flow regime map for the Type A inlet and (b) its comparison with that in literature.

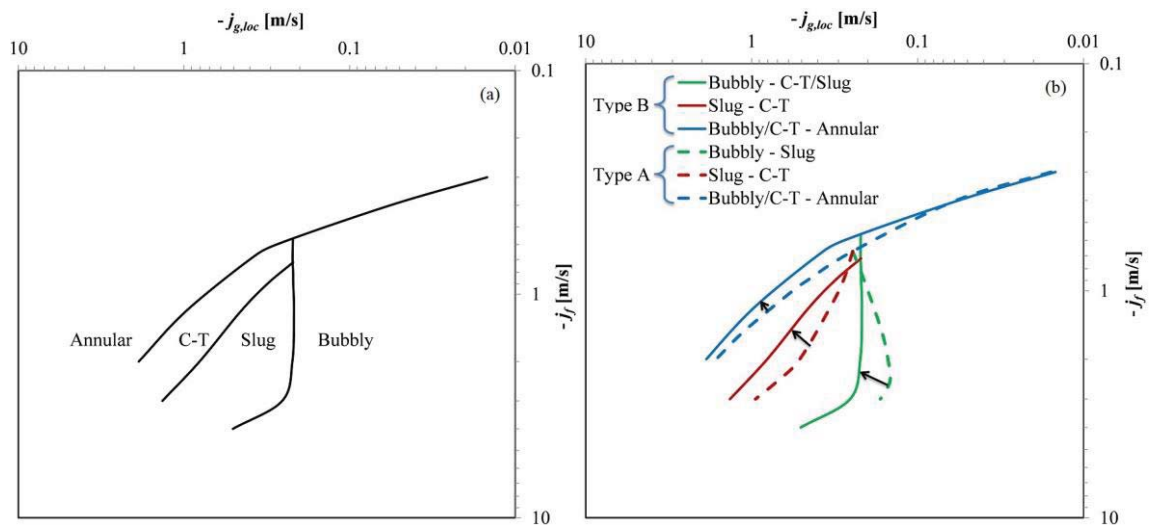
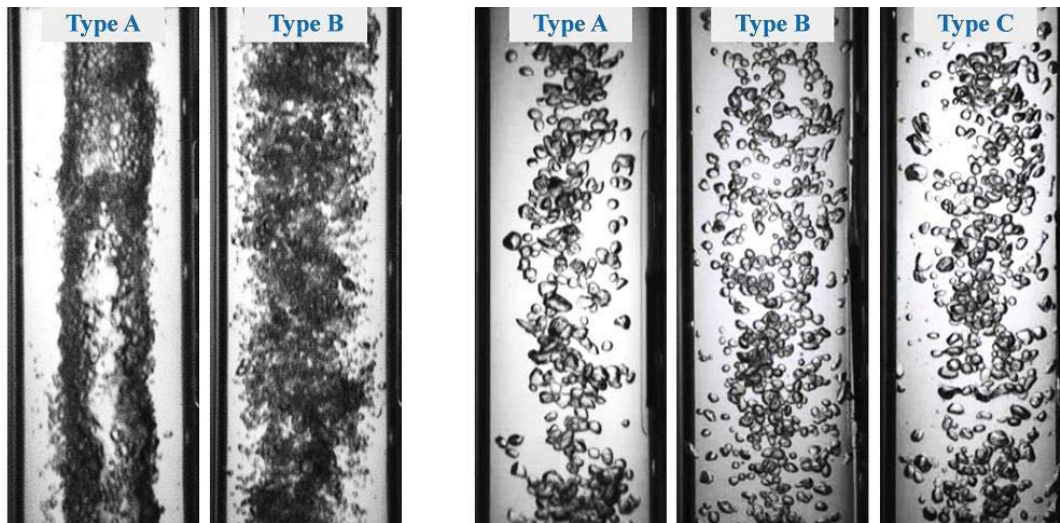


Figure 5. (a) Flow regime map for the Type B inlet and (b) its comparison with the Type A inlet.

To confirm the effect of reduced coring by the flow straightener, images at port P15 for Run 3 and at ports P13 and P9 for Run 1 are shown in Fig. 6, respectively. As can be seen from the images, near the inlet at port P15, a gas core is observed for Type A inlet while dispersed bubbly flow is observed for the Type B inlet. Similarly, far downstream at port P13, bubbles are more distributed around the pipe cross-section for the Type B inlet, while they are more agglomerated at the pipe center for the Type A inlet. The comparison indicates that the flow straightener can significantly reduce the coring phenomenon in the vertical-downward two-phase flow. Since coring is reduced, bubble distribution becomes more dispersed and the probability for coalescence decreases. As a result the transition boundaries for different flow regimes are shifted to higher superficial gas velocities.



(a) Near the inlet ($-j_{g,loc}=0.284$ m/s) (b) Far downstream from the inlet ($-j_{g,loc}=0.108$ m/s)
 Figure 6. Images near and far downstream from the inlet for $-j_f = 4.00$ m/s.

Fig. 7 shows the flow regime map for the Type C inlet and the comparison of the flow regime map between Type A and Type C inlets. Several observations can be made from the comparison: (1) the transition boundaries from slug to churn-turbulent flow and churn-turbulent to annular flow are shifted to higher superficial gas velocities; (2) the transition boundary from bubbly to slug flow, however, behaves differently from that in the Type A inlet. This boundary is shifted to higher superficial gas velocity when superficial liquid velocity is greater than 2.5 m/s while the shift is opposite for superficial liquid velocity is less than 2.5 m/s. This can be explained on the basis of inlet condition. Intermittent flows serve as the inlet at low superficial liquid velocities, which causes the flow to favorably develop into slug flow. While at higher superficial liquid velocity, bubbly flow serves as inlet. With the reduced coring observed from Fig. 6 (b) for the Type C inlet, it would require a longer development length for the dispersed bubbles to agglomerate at the center of the pipe and coalesce into slug bubbles. Therefore, the transition from bubbly to slug flow occurs much later. It should be noted that in the current study, counter-current flow is not investigated; therefore no kinematic shock is indicated in the flow regime map.

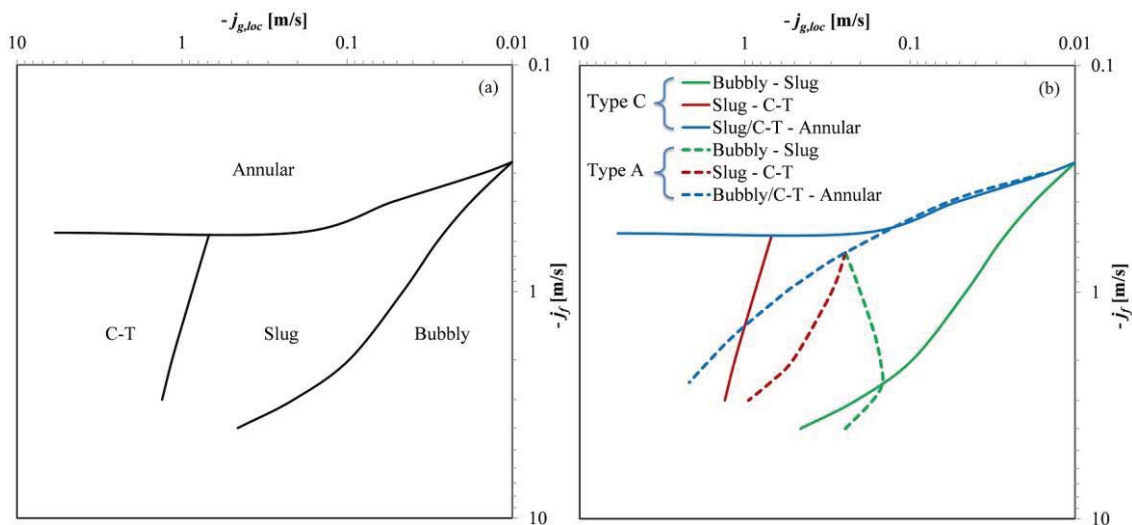


Figure 7. (a) Flow regime map for the Type C inlet and (b) its comparison with the Type A inlet.

3.2. Frictional Pressure Loss Analysis

The Lockhart-Martinelli method [10] is used to assess the two-phase frictional pressure loss in the vertical-downward two-phase flow with three types of inlets, as shown in Fig. 8. From the figure, the pressure loss for Type B and Type C inlets are similar. Both can be correlated well by a coefficient C value of 25, which is greater than the conventional value of 20. This indicates that the pressure loss is slightly higher than that observed in the vertical-upward flow. However, the result for Type A inlet is yet conclusive. In the current analysis, the data is correlated with a C value of approximately 100. This may suggest that the additional pressure loss in Type A inlet may be induced from the significant coring and rotation of the flow. However, the fluctuation in the data with C=100 may indicate that additional study may be needed to model the frictional pressure loss under such inlet condition as Type A.

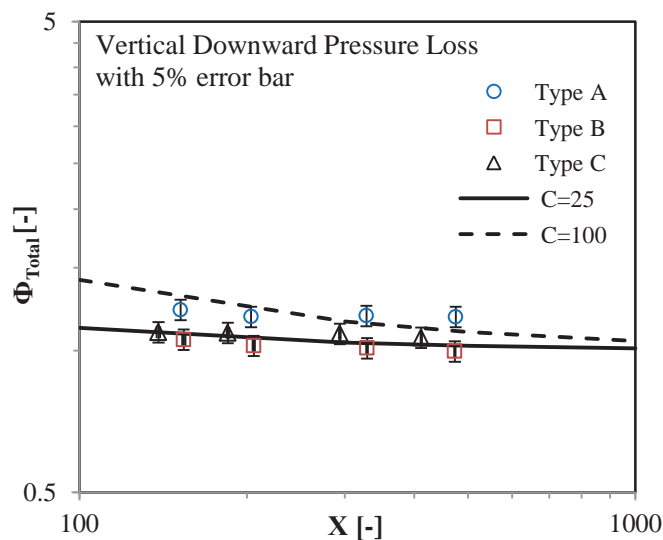


Figure 8. Frictional pressure analysis using the Lockhart-Martinelli method.

3.3. Interfacial Structures in the Vertical-downward Section

The time-averaged local two-phase flow parameters are acquired by the state-of-the-art four-sensor conductivity probe, which has an accuracy of approximately $\pm 7\%$. Experiments are performed at three axial locations in the vertical test sections for each injector type. For Type A and Type B inlets, the local parameters are measured at ports P15, P14, and P13 which are located at $L/D = 7.5, 31.5,$ and $55.5,$ respectively, from injector II. For the Type C injector, the local parameters are measured at ports P7, P8, and P9 which are located at $L/D = 3, 16.5,$ and $67.5,$ respectively, from the vertical-downward elbow.

To assess the accuracy of the conductivity probe measurement, the superficial gas velocity at each port determined from the probe measurements $\langle \alpha v_g \rangle$ is compared with $\langle j_g \rangle_z$ obtained from gas rotameter and local pressure measurement. Here, $\alpha, v_g,$ and the brackets denote the void fraction, the bubble velocity, and the area-average operator, respectively. As shown in Fig. 9, for most of the flow conditions, the two measurements agree well within $\pm 10\%$ difference. It should be noted that at high superficial gas velocity (i.e., Run 3 and Run 4), the Type A inlet creates a gas jet that extends to port P14 ($L/D = 31.5$). For the Type B inlet, the gas jet is eliminated but gas pockets are still observed at port P15. Under such flow conditions there could be large uncertainty in the conductivity probe measurement.

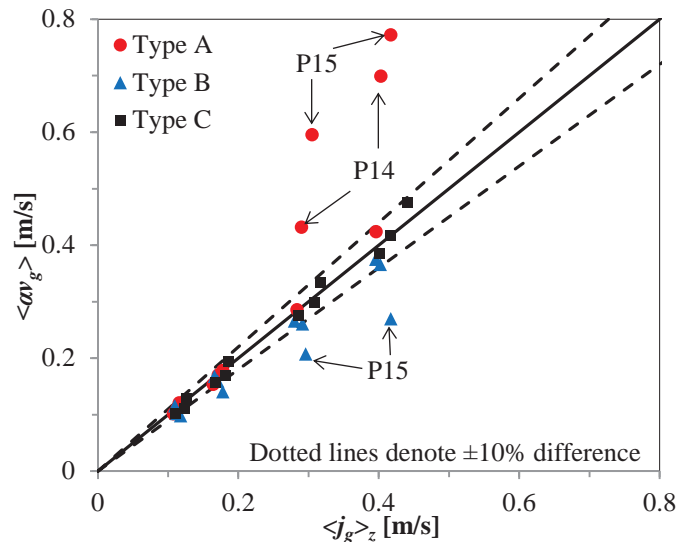


Figure 9. Comparison between the measurements by the flow meter and the conductivity probe.

3.3.1. Type A inlet

For the injector without the flow straightener (Type A inlet), local measurements are obtained at ports P15, P14, P13, which are located at 7.5D, 31.5D, and 55.5D downstream from the inlet. The bubble distribution is confirmed to be axisymmetric in the vertical-downward section by taking data at two perpendicular pipe diameters, and therefore, local measurements are only taken along one diameter of the pipe cross-section.

Fig. 10 and Fig. 11 show the development of the local void fraction and interfacial area concentration profiles along the test section for Run 1 and Run 3, respectively. The void fraction profile peaks at the center of the pipe which is consistent with the coring phenomenon observed in the flow visualization. This is different from the void distribution in the upward flow which usually has a wall-peaked void profile. In the downward flow, the bubbles move slower than the liquid due to the buoyancy force acting in the direction opposite to the direction of the main flow, while the opposite is observed in the upward flow. Since the lift force is proportional to the product of the radial gradient of the axial velocity of the continuous phase and the relative velocity, the direction of the lift force is opposite for upward and downward flows [6]. In addition, center-peaked void distribution is enhanced near the inlet by the Type A injector. As the flow develops downstream, the effects of the inlet dissipate and coring phenomenon is reduced, therefore, causing the void fraction profile to become flatter in shape.

For bubbly flows, the interfacial area concentration is proportional to the void fraction and inversely proportional to the bubble Sauter-mean diameter. Therefore, the radial profiles of the void fraction and interfacial area concentration are quite similar in bubbly flows, which is the case for Run 1 and Run 2. However, the relatively high superficial gas velocity of Run 3 and Run 4 cause an air jet to be formed just downstream of the inlet (as shown earlier in Fig. 6(a)) due to the gas occupying the majority of the inner annulus of the two-phase injector unit, and it is well highlighted by the void fraction profile in Fig. 11(a). As a result, the interfacial area concentration in such a condition shows a significant decrease at the center of the pipe and peaks at approximately $r/R = \pm 0.4$ as shown in Fig. 11(b). As the flow develops, however,

the gas core disintegrates into smaller bubbles due to coring and gravity effects, and typical center-peaked void fraction and interfacial area concentration profiles are observed at ports P13 and P14.

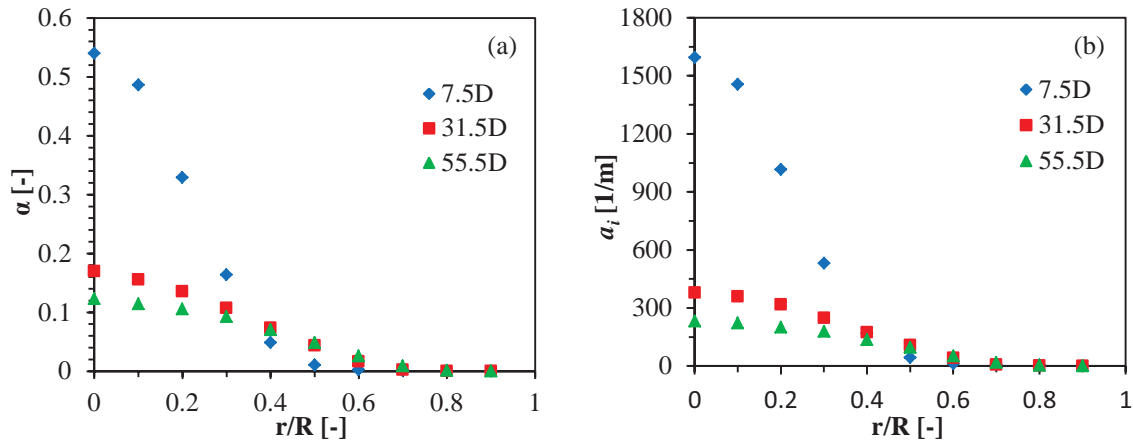


Figure 10. Local parameter profiles for Run 1 ($-j_f=4.00$ m/s, $-j_{g,loc}=0.108$ m/s) with the Type A inlet. (a) void fraction (b) interfacial area concentration

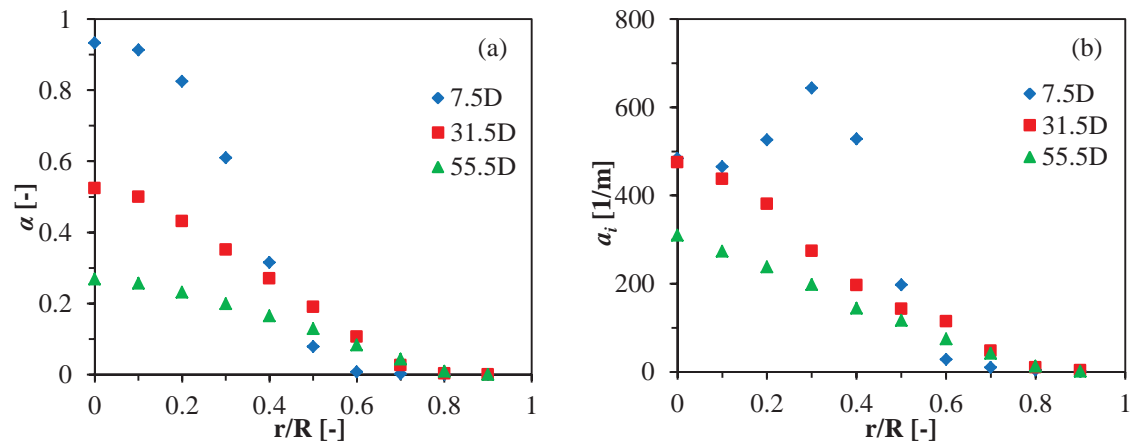


Figure 11. Local parameter profiles for Run 3 ($-j_f=4.00$ m/s, $-j_{g,loc}=0.284$ m/s) with the Type A inlet. (a) void fraction (b) interfacial area concentration

3.3.2. Type B inlet

For the Type B inlet, a flow straightener is added to the injection system to reduce the rotation of the two phases caused by the injection of the water. Local measurements are obtained at ports P15, P14, and P13, which are located at 7.5D, 31.5D, and 55.5D downstream from the inlet, respectively.

The local profiles of the two-phase flow parameters at different axial locations and for increasing gas flow rate are shown in Fig. 12. It is observed that the placement of the honeycomb flow straightener in the outer annulus of the injector system significantly changes the development of the radial profiles of the void fraction and interfacial area concentration along the test section when compared to the Type A inlet. As shown in the figure, the void fraction and interfacial area concentration profiles still show center-peaked shapes caused by the lift force. However, the coring is reduced especially at the port near the injector since the peak is significantly reduced. Furthermore, different from the Type A inlet, the void

fraction and interfacial area concentration maintain the relatively same magnitude and center-peaked shape as the flow develops along the test section. This phenomenon may be due to the effects of the flow straightener which reduces interactions between bubbles by reducing turbulence. As a result, flow develops within a short axial length and bubble interactions are subdued.

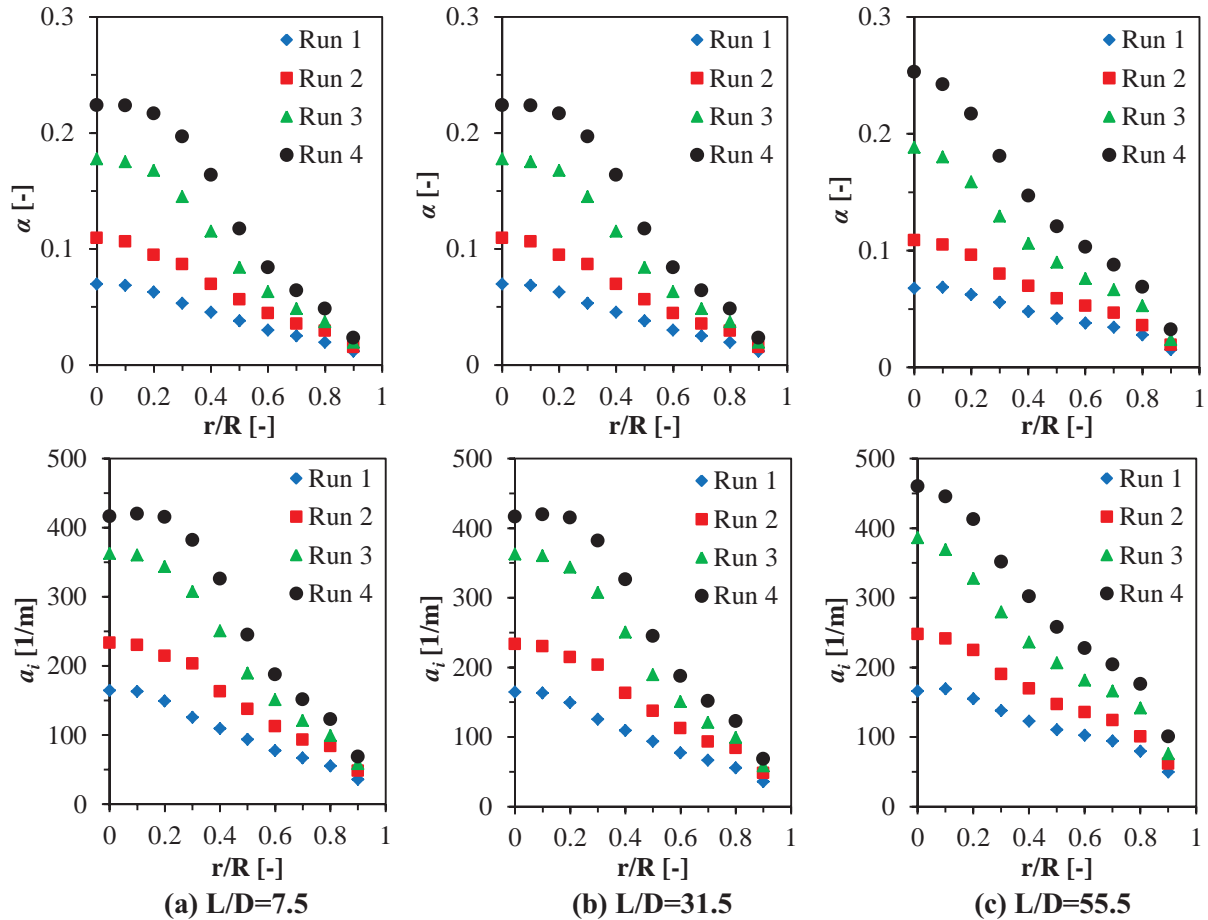


Figure 12. Local void fraction and interfacial area concentration profiles along the test section.

3.3.3. Type C inlet

For the vertical-downward elbow inlet (Type C inlet), the local two-phase flow parameters are measured at port P7, P8, and P9, which are located at 3D, 16.5D, and 67.5D from the elbow. As previously discussed, the flow is asymmetrical at port P7, and local data is acquired in four different radial directions, leading to a total of 60 data points across the pipe cross-section.

Fig. 13 shows the three-dimensional surface plots of the void fraction and interfacial area concentration generated in MATLAB by using the cubic interpolation of the measured data from Run 1. As can be observed from the figure, the local profiles peak towards the inner curvature of the elbow, which suggests that the bubbles migrate into this region. Although the secondary flow observed by previous researches is expected [11,12], higher inertia driven by the liquid phase forces it to travel along the outside curvature of the elbow, and hence, driving the lighter phase towards the elbow's inner curvature. As evident from Fig. 14, the inlet effects of elbow decays by port P8 ($L/D=16.5$), and the flow becomes axisymmetric along the pipe cross-section. As the flow develops, the void fraction and interfacial area concentration become more

uniform and form center-peaked profiles due to the coring phenomenon characteristic of vertical-downward bubbly two-phase flow as shown in the figure.

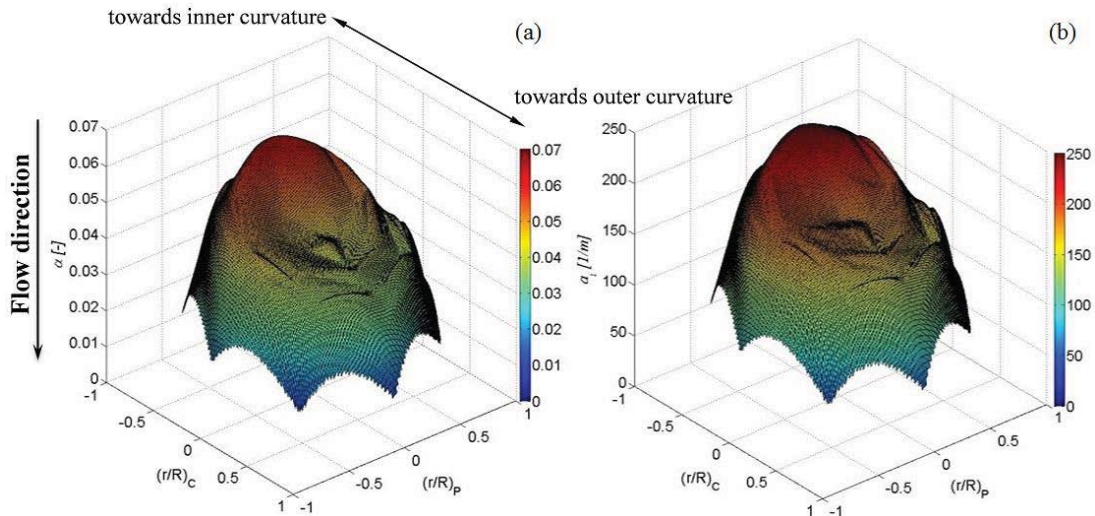


Figure 13. Local surface plots at port 7 ($L/D=3$) for Run 1 ($-j_f=4.00$ m/s, $-j_{g,loc}=0.108$ m/s). (a) void fraction (b) interfacial area concentration

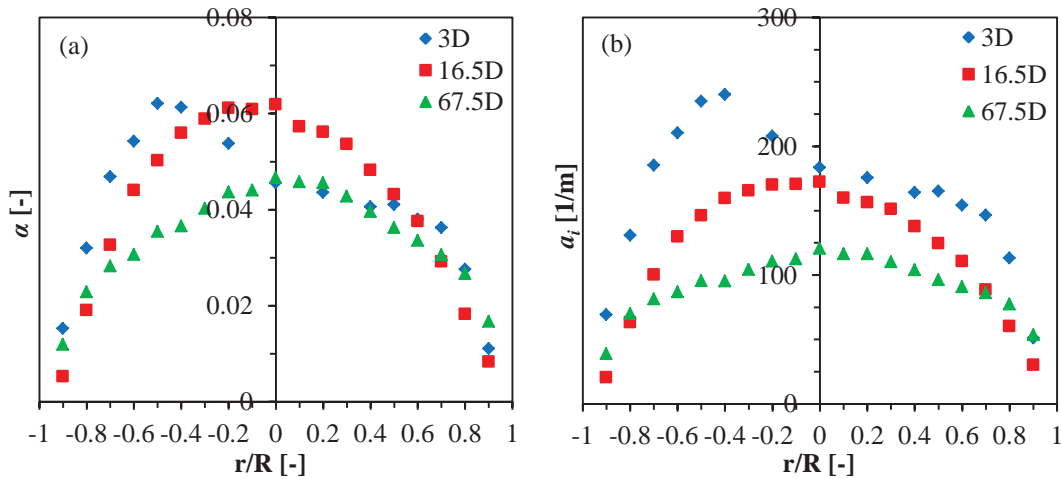


Figure 14. Local profiles for Run 1 ($-j_f=4.00$ m/s, $-j_{g,loc}=0.108$ m/s). (a) void fraction (b) interfacial area concentration ($L/D=3$ indicates the profiles along $\theta=0^\circ$ or r/R_C)

Overall, the vertical-downward two-phase flow has a typical center-peaked void profile as opposed to a wall-peaked profile observed in vertical-upward flow. This is believed to be caused by the change in direction of the lift force. Furthermore, it is shown that the Type A inlet results in the most pronounced center-peaked void fraction profile, due to the significant coring effect created by the two-phase flow injector as observed from the flow visualization. Type B and Type C inlet provide more uniform distributions of the void fraction profiles with reduced coring effect.

4. CONCLUSIONS

In the present study, the effects of three types of inlets in co-current vertical-downward air-water two-phase flow are studied using flow visualization approach, frictional pressure loss analysis, and local interfacial structures analysis.

First, a detailed flow visualization study is performed. Flow regimes including bubbly, slug, churn-turbulent, and annular flow are defined, and flow regime maps are developed for each inlet configuration. Through flow visualization, it is found that vertical-downward two-phase flow has a typical center-peaked void distribution primarily caused by the lift force. The comparisons of the flow regimes maps show that Type A inlet results in a gas core near the inlet and form significant coring effect even in the downstream of the flow. Type B and Type C inlets can reduce the coring effect to a certain degree thereby reducing bubble coalescence and shifting the regime transition boundaries to higher superficial gas velocities.

Second, Lockhart-Martinelli method is used to study the two-phase frictional pressure loss in different types of inlets. The result indicates that Lockhart-Martinelli correlation is capable of correlating the two-phase frictional pressure loss for the Type B and Type C inlets with coefficient C value of 25 with an accuracy of $\pm 5\%$. For the Type A inlet, the pressure loss is found to be higher. The additional pressure loss is expected to be caused by the significant coring effect. A coefficient C value of 100 is correlated to the experimental data. However, additional study may need to be performed.

Finally, local two-phase flow parameters are acquired by using a four sensor conductivity probe. The local data shows a center-peaked void profile which is consistent with the coring phenomenon observed by flow visualization. Downstream from the inlet, the Type A inlet results in the most pronounced center-peaked void fraction profile while the profile is more uniform for Type B and Type C inlets. Moreover, asymmetric bubble distribution occurs just after the Type C inlet due to the high liquid inertia.

REFERENCES

1. T. Oshinowo and M. E. Charles, "Vertical two-phase flow part I. Flow pattern correlations," *Can. J. Chem. Eng.*, **52**, pp. 25–35, (1974).
2. K. Usui and K. Sato, "Vertically Downward Two-Phase Flow, (I)," *Journal of Nuclear Science and Technology*, **26**(7), pp. 670–680, (1989).
3. D. Barnea et al., "Flow pattern transition for vertical downward two phase flow," *Chem. Eng. Sci.*, **37**, pp. 741–744, (1982).
4. H. Goda et al., "Flow Regime Identification of Co-Current Downward Two-Phase Flow with Neural Network Approach," *10th International Conference on Nuclear Engineering*, Vol. **3**, pp. 1–8, (2002).
5. H. Goda et al., "Local Interfacial Structure in Downward Two-Phase Bubbly Flow," *10th International Conference on Nuclear Engineering*, Vol. **3**, pp. 115–121, (2002).
6. M. Ishii et al., "Interfacial structures and interfacial area transport in downward two-phase bubbly flow," *Int. J. Multiph. Flow*, **30**(7), pp. 779–801, (2004).
7. S. Kim et al., "Interfacial Structures and Regime Transition in Co-Current Downward Bubbly Flow," *J. Fluids Eng.*, **126**, p. 528, (2004).
8. S. M. Bhagwat and A. J. Ghajar, "Similarities and differences in the flow patterns and void fraction in vertical upward and downward two phase flow," *Exp. Therm. Fluid Sci.*, **39**, pp. 213–227, (2012).
9. S. Kim et al., "Development of the miniaturized four-sensor conductivity probe and the signal processing scheme," *Int. J. Heat Mass Transf.*, **43**, pp. 4101–4118, (2000).
10. R. W. Lockhart and R. c. Martinelli, "Proposed correlation of data for isothermal two-phase, two-component flow in pipes," *Chemical Engineering Progress*, **45**, pp. 39–48, (1949).
11. M. S. Yadav et al., "Experiments on geometric effects of 90-degree vertical-upward elbow in air water two-phase flow," *Int. J. Multiph. Flow*, **65**, pp. 98–107, (2014).
12. M. S. Yadav et al., "Characterization of the dissipation of elbow effects in bubbly two-phase flows," *Int. J. Multiph. Flow*, **66**, pp. 101–109, (2014).